Neuron

Report

Developmental reprogramming in melanocortin neurons modulates diet-induced obesity in mice

Graphical abstract

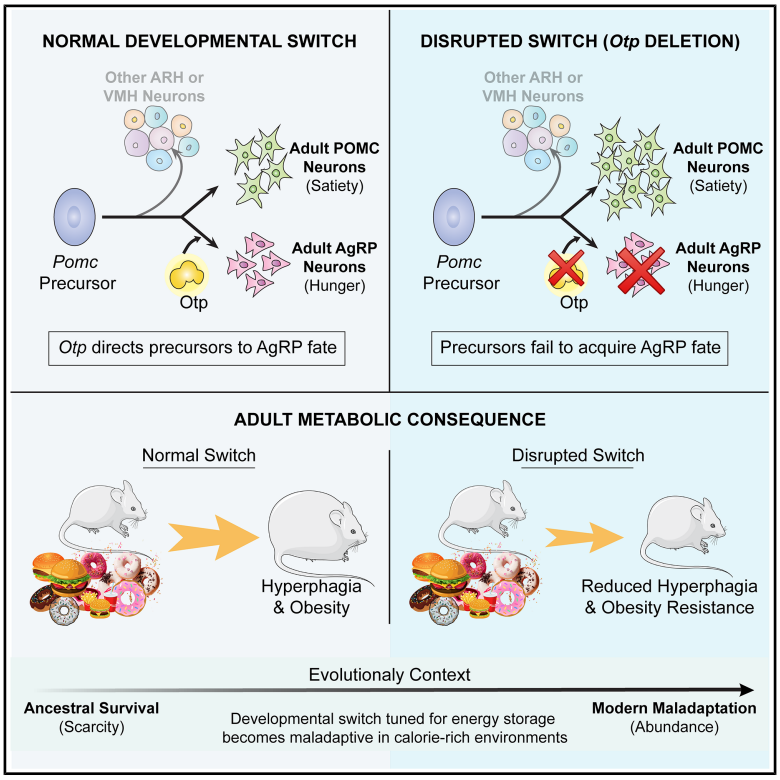

Highlights

- *Pomc* precursors give rise to diverse neuronal subtypes in the adult ARH and VMH
- *Otp* directs the developmental fate switch from POMC to AgRP neurons
- This fate switch shapes sex-dependent susceptibility to obesity in adult mice

Authors

Baijie Xu, Li Li, Meilin Chen, ..., Amanda G. Almeida, Steven C. Wyler, Chen Liu

Correspondence

chen.liu@utsouthwestern.edu

In brief

Xu et al. show that a developmental "switch" in the hypothalamus determines whether immature neurons become appetite suppressing or appetite stimulating. Disrupting this switch reshapes feeding behavior and protects mice from obesity, revealing how early-life programming shapes lifelong metabolic health.

Xu et al., 2026, Neuron *114*, 1–9
April 1, 2026
https://doi.org/10.1016/j.neuron.2025.12.022

CellPress

Please cite this article in press as: Xu et al., Developmental reprogramming in melanocortin neurons modulates diet-induced obesity in mice, Neuron (2025), https://doi.org/10.1016/j.neuron.2025.12.022

Neuron

CellPress
OPEN ACCESS

Report

Developmental reprogramming in melanocortin neurons modulates diet-induced obesity in mice

Baijie Xu,[1,4] Li Li,[1,4,5] Meilin Chen,[1] Zan Wu,[1] Xiameng Chen,[1] Swati,[1] Rong Wan,[1] Amanda G. Almeida,[1] Steven C. Wyler,[1] and Chen Liu[1,2,3,6,*]

[1]The Hypothalamic Research Center, Department of Internal Medicine, UT Southwestern Medical Center, Dallas, TX 75390, USA
[2]Department of Neuroscience, UT Southwestern Medical Center, Dallas, TX 75390, USA
[3]Peter O'Donnell Jr. Brain Institute, UT Southwestern Medical Center, Dallas, TX 75390, USA
[4]These authors contributed equally
[5]Present address: Department of Zoology and Physiology, University of Wyoming, Laramie, WY 82071, USA
[6]Lead contact
*Correspondence: chen.liu@utsouthwestern.edu
https://doi.org/10.1016/j.neuron.2025.12.022

SUMMARY

Central melanocortin neurons are essential regulators of energy balance in mammals. Specifically, hypothalamic proopiomelanocortin (POMC) neurons promote satiety, while agouti-related peptide (AgRP) neurons drive hunger. Despite their well-understood roles in adulthood, the developmental processes that shape this system remain poorly understood. *Pomc*-expressing precursors give rise to multiple neuronal subtypes, including a subset of adult AgRP neurons, but the precise mechanisms guiding these fate transitions—and their lasting impact on metabolic health—have remained unknown. Here, we show that the transcription factor *Otp* directs a developmental fate switch between POMC and AgRP neuron identities. Loss of *Otp* in *Pomc*-expressing precursors disrupts this switch, altering the balance of anorexigenic and orexigenic neurons in the adult hypothalamus. This developmental event is critical for programming susceptibility to diet-induced obesity in mice. Our findings highlight the remarkable plasticity within the developing melanocortin system and underscore the importance of using refined genetic tools to target these neurons more precisely.

INTRODUCTION

The central melanocortin neurons regulate satiety in mammalian species.[1] Proopiomelanocortin (POMC) and agouti-related peptide (AgRP) neurons in the arcuate nucleus of the hypothalamus (ARH) play crucial and opposing roles in regulating food intake. POMC neurons promote satiety by releasing the anorexigenic peptide α-melanocyte-stimulating hormone (α-MSH), while AgRP neurons promote hunger through the orexigenic peptides AgRP and neuropeptide Y (NPY), as well as the inhibitory neurotransmitter γ-aminobutyric acid (GABA).[2] While functionally distinct, these neurons arise, in part, from shared neuronal precursors during development.[3] In mice, *Pomc* mRNA first appears in the developing hypothalamus at embryonic day (E)10.5.[4] The number of *Pomc*-expressing neurons gradually increases, reaching a peak around E13.5.[3] However, *Pomc* expression in these neurons does not dictate terminal cell fate. Instead, more than half of them lose *Pomc* expression as they adopt other peptidergic identities by the early postnatal period. Remarkably, some *Pomc* precursors begin expressing *Npy*, a marker for AgRP neurons, giving rise to a subset of adult AgRP neurons.[3] Despite these observations, the molecular mechanisms governing the developmental fate switch between two functionally antagonistic feeding neuron populations and its long-term physiological consequences have remained unknown.

Beyond *Agrp*, recent studies indicate that *Pomc* precursors express other cell fate markers during embryonic and early postnatal periods.[5] Yet, the full identity and spatial distribution of POMC-derived neurons in the adult mediobasal hypothalamus, especially those no longer expressing *Pomc*, have not been systematically characterized. This gap is significant, as *Pomc-Cre* mice are widely used to perturb gene expression in POMC neurons, with resulting phenotypical effects often attributed solely to changes within these specific neurons. However, as with endogenous *Pomc*, *Cre* recombinase driven by the *Pomc* promoter also targets non-POMC neurons,[6,7] potentially confounding data interpretation.

RESULTS

Identifying the POMC-derived neurons in the adult mouse mediobasal hypothalamus

We conducted single-nucleus multi-omic profiling of *Pomc*-lineage neurons (hereafter referred to as PL neurons) in the adult mediobasal hypothalamus (Figure 1A). To label PL neurons, we generated double transgenic mice (*Pomc-Cre; R26*$^{LSL\text{-}Sun1\text{-}sfGFP}$),

Please cite this article in press as: Xu et al., Developmental reprogramming in melanocortin neurons modulates diet-induced obesity in mice, Neuron (2025), https://doi.org/10.1016/j.neuron.2025.12.022

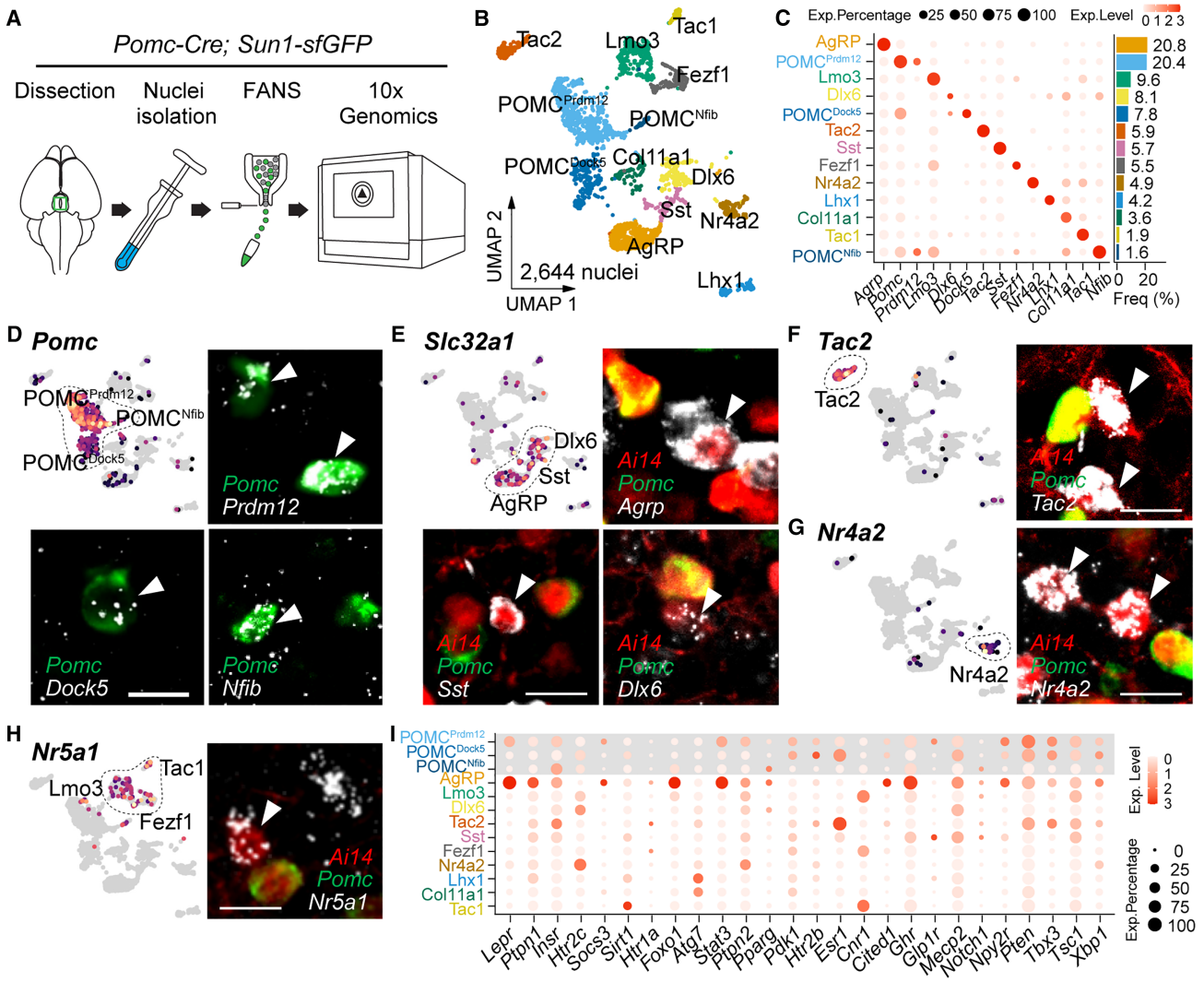

Figure 1. Single-nuclei multiome analyses of POMC-derived neurons in the adult mouse mediobasal hypothalamus

(A) Schematic of isolating and purifying PL neurons for single-nuclei ATAC and gene expression analyses.

(B) Uniform manifold approximation and projection (UMAP) plot showing 13 PL neuron clusters from 2,644 nuclei.

(C) Left: dot plot of marker gene expression across clusters. Dot size represents the percentage of expressing cells, and color indicates expression levels (light: low, dark: high). Right: bar plot showing the distribution of PL neuron clusters, with percentages indicated.

(D) Feature plot showing expression of *Pomc* in POMC^{Prdm12}, POMC^{Dock5}, and POMC^{Nfib} clusters verified by RNAscope, highlighting the co-expression of *Pomc* with *Prdm12*, *Dock5*, and *Nfib* mRNAs in individual neurons (arrowheads). Scale bar: 20 μm.

(E) Feature plot showing expression of vesicular GABA transporter *Slc32a1* in three GABAergic PL neuron clusters lacking *Pomc* expression. RNAscope analyses verified the expression of *Agrp*, *Sst*, and *Dlx6* in individual PL neurons (arrowheads) labeled by *Pomc-Cre* activated tdTomato (Ai14) fluorescence. Scale bar: 20 μm.

(F and G) Feature plots showing the expression of *Tac2* (F) and *Nr4a2* (G) in PL neuron clusters lacking *Pomc*. RNAscope analyses verified the expression of *Tac2* (F) and *Nr4a2* (G) in individual PL neurons (arrowheads). Scale bars: 20 μm.

(H) Feature plot showing the expression of *Nr5a1* in three PL neuron clusters, verified by RNAscope (arrowheads). Scale bars: 20 μm.

(I) Dot plot illustrates the relative expression of genes targeted by *Pomc-Cre* across PL neurons, with dot size proportional to the percentage of expressing cells and colors indicating expression levels (light: low, dark: high).

See also Figures S1–S5.

in which PL neurons were permanently marked by the expression of a nuclear GFP (*Sun1-sfGFP*).[8] Under a stereomicroscope, we isolated the mediobasal hypothalamus from adult mice and extracted and purified GFP^{+} nuclei via fluorescence-activated nuclei sorting (FANS).[9]

Integrated chromatin accessibility and gene expression analyses of 2,644 PL neurons revealed 13 transcriptionally distinct subpopulations (Figures 1B and 1C). Cross-validations with recent datasets of developing and mature *Pomc*-expressing neurons confirmed the reproducibility of key neuronal populations[5,10]

Please cite this article in press as: Xu et al., Developmental reprogramming in melanocortin neurons modulates diet-induced obesity in mice, Neuron (2025), https://doi.org/10.1016/j.neuron.2025.12.022

(Figure S1). Remarkably, only three clusters (POMC^{Prdm12}, POMC^{Dock5}, and POMC^{Nfib}) retained *Pomc* expression, collectively representing 29.8% of all PL neurons in the adult mediobasal hypothalamus (Figures 1D and S2A–S2C). Consistent with previous single-cell analyses of adult POMC neurons,[10–12] these clusters differ in *Pomc* expression levels: POMC^{Prdm12} neurons exhibit the highest expression, whereas POMC^{Dock5} and POMC^{Nfib} neurons show lower levels (Figures 1C and S1B).

Given that arcuate GABAergic neurons play critical roles in energy metabolism,[13,14] we next examined PL-derived GABAergic clusters and identified three—AgRP, somatostatin (Sst), and distal-less homeobox 6 (Dlx6)—that lacked *Pomc* expression (Figures 1E and S2D–S2F). Among these, AgRP neurons accounted for 20.8% of all PL neurons, representing the largest non-POMC cluster (Figure 1C). Recent studies have shown that arcuate *Agrp*-negative *Npy* and *Npy/Pnoc* neurons also contribute to energy homeostasis.[15,16] Interestingly, we detected a small number of such neurons within POMC-derived populations; however, these were sparsely distributed outside the AgRP cluster (Figure S3A). By contrast, within the AgRP cluster, co-expression of *Agrp* and *Npy* was highly robust, with 95% of neurons expressing both transcripts (Figure S3B), validating *Npy* as a reliable marker for the vast majority of POMC-derived AgRP neurons.

PL neurons were also found in other well-characterized ARH neuronal populations, such as Tac2/Kiss1 and Nr4a2/TH neurons (Figures 1F, 1G, S2G, and S2H), which are known to regulate reproduction and feeding.[17,18] Unexpectedly, three PL neuron clusters (Lmo3, Fezf1, and Tac1) exhibit molecular signatures characteristic of ventromedial hypothalamus (VMH) neurons. These neurons express the VMH neuron marker *Nr5a1* (also known as *Sf1*; Figures 1H and S2I). Histological analyses confirmed that they are located within the VMH or near the VMH/ARH boundary (Figure S4). Together, these findings demonstrate that *Pomc* precursors give rise to multiple ARH and VMH neuron subtypes with diverse physiological functions.

A PubMed search revealed that *Pomc-Cre* has been used to manipulate at least 80 different genes. Examination of the expression patterns of these genes across PL neuron clusters showed that none are exclusively expressed in *Pomc*-expressing neurons in the adult hypothalamus (Figures 1I and S5A). For example, the cannabinoid receptor *Cnr1* is predominantly found in non-POMC PL neuron clusters (Figures 1I and S5B). Additionally, the leptin receptor *Lepr* and its downstream signaling molecules, *Stat3* and *Socs3*, show robust expression in the AgRP cluster (Figures 1I and S5C). Other key metabolic sensors and regulators, including the insulin and serotonin receptors, as well as genes involved in endoplasmic reticulum (ER) stress and mammalian target of rapamycin (mTOR) pathways, are also expressed in various non-POMC PL neurons that are nonetheless targeted by *Pomc-Cre* (Figures 1I, S5D, and S5E).

Otp is necessary for *Agrp* expression in the adult ARH

Cell counting in *Pomc-Cre; Ai14; Npy-GFP* mice revealed that 54% of adult AgRP neurons (*Npy-GFP*$^+$) arise developmentally from *Pomc* precursors (*Pomc-Cre*$^+$*; Ai14*$^+$; Figure 2A). Since neuronal identity is governed by distinct gene regulatory networks (GRNs),[19] we analyzed single-nucleus chromatin accessibility and gene expression data to identify enhancer-driven transcriptional networks enriched in specific PL neuron clusters.[20] In POMC-derived AgRP neurons, we identified GRNs coordinated by six transcriptional regulators: *Otp*, *Nr3c1*, *Foxo1*, *Stat3*, *Crem*, and *Esrrg* (Figures 2B and S6A). Notably, unlike the others, the expression of the homeodomain transcription factor *Otp* is largely restricted to the AgRP cluster (Figure S6B). Immunostaining further confirmed that Otp is present in all adult AgRP neurons, regardless of their developmental origin, but is absent from neurons expressing *Pomc* (Figures 2C, 2D, and S7).

To determine whether *Otp* is required for *Agrp* expression, we injected adeno-associated viruses (AAVs) expressing *Cre* recombinase into the ARH of adult *Otp*$^{fl/fl}$ mice (Figure 2E). 3 weeks after injection, Otp protein was undetectable in the ARH of these mice (Figure 2F), accompanied by a near-complete loss of *Agrp* mRNA (Figure 2G), while the number of POMC neurons remained unchanged (107.8% ± 7.3%, $p = 0.39$ vs. control, $n = 6$ mice; Figure 2G). Next, we injected *Cre*-dependent *Otp* constructs into the ARH of *Pomc-Cre* mice (Figure 2H). Ectopic Otp expression was evident in AAV-targeted POMC neurons (GFP$^+$; Figure 2I) and resulted in a significant reduction in *Pomc* expression in the ARH compared with control AAVs (Figure 2J), whereas the number of AgRP neurons remained constant (95.4% ± 10.4%, $p = 0.72$ vs. control, $n = 4$ mice; Figure 2J). Notably, neither *Otp* deletion nor overexpression in adult ARH neurons led to increased cell death (Figure S8). Together, these findings indicate that Otp promotes *Agrp* expression while repressing *Pomc* in the adult ARH.

Otp is necessary for the POMC-to-AgRP fate switch

The developmental transition from *Pomc* to *Npy* expression, marking prospective AgRP neurons, occurs between E14 and E18, during which some PL neurons transiently co-express *Pomc* and *Npy*.[3] We detected *Otp* mRNA in *Pomc*-expressing neurons in E15.5 embryos.[21] Notably, none of the *Pomc* precursors (*Pomc-Cre*$^+$*; Ai14*$^+$) express Otp or *Npy-GFP* at E13.5 (Figure 3A). However, by E14.5, a subset of *Pomc* precursors (35.6% ± 3.0%; Figure 3A) began to express Otp, coinciding with the initial appearance of *Npy-GFP* in these neurons (Figure 3A).

To determine whether *Otp* is required for the POMC-to-AgRP fate switch, we generated *Pomc-Cre; Otp*$^{fl/fl}$ mice, in which the onset of *Otp* expression is blocked in *Pomc* precursors (hereafter referred to as *Otp*$^{Pomc\ KO}$ mice). In *Otp*$^{Pomc\ KO}$*; Npy-GFP* mice, the total number of PL neurons (*Pomc-Cre*$^+$*; Ai14*$^+$) was comparable to that of controls (Figures 3B–3D), indicating that *Otp* is not required for cell survival. However, there was a significant loss of POMC-derived AgRP neurons (*Pomc-Cre*$^+$*; Ai14*$^+$, *Npy-GFP*$^+$), while the number of non-POMC-derived AgRP neurons (*Npy-GFP*$^+$*; Pomc-Cre*$^-$) remained unaffected (Figures 3B–3D). Furthermore, single-nucleus analyses of PL neurons in adult *Otp*$^{Pomc\ KO}$ mice revealed a marked reduction in the AgRP cluster, accompanied by an expansion of the POMC^{Dock5} population (Figure 3E). Other PL neuron clusters, including POMC^{Prdm12} and POMC^{Nfib} neurons, remained unchanged. Consistent with these changes in PL neuron

Please cite this article in press as: Xu et al., Developmental reprogramming in melanocortin neurons modulates diet-induced obesity in mice, Neuron (2025), https://doi.org/10.1016/j.neuron.2025.12.022

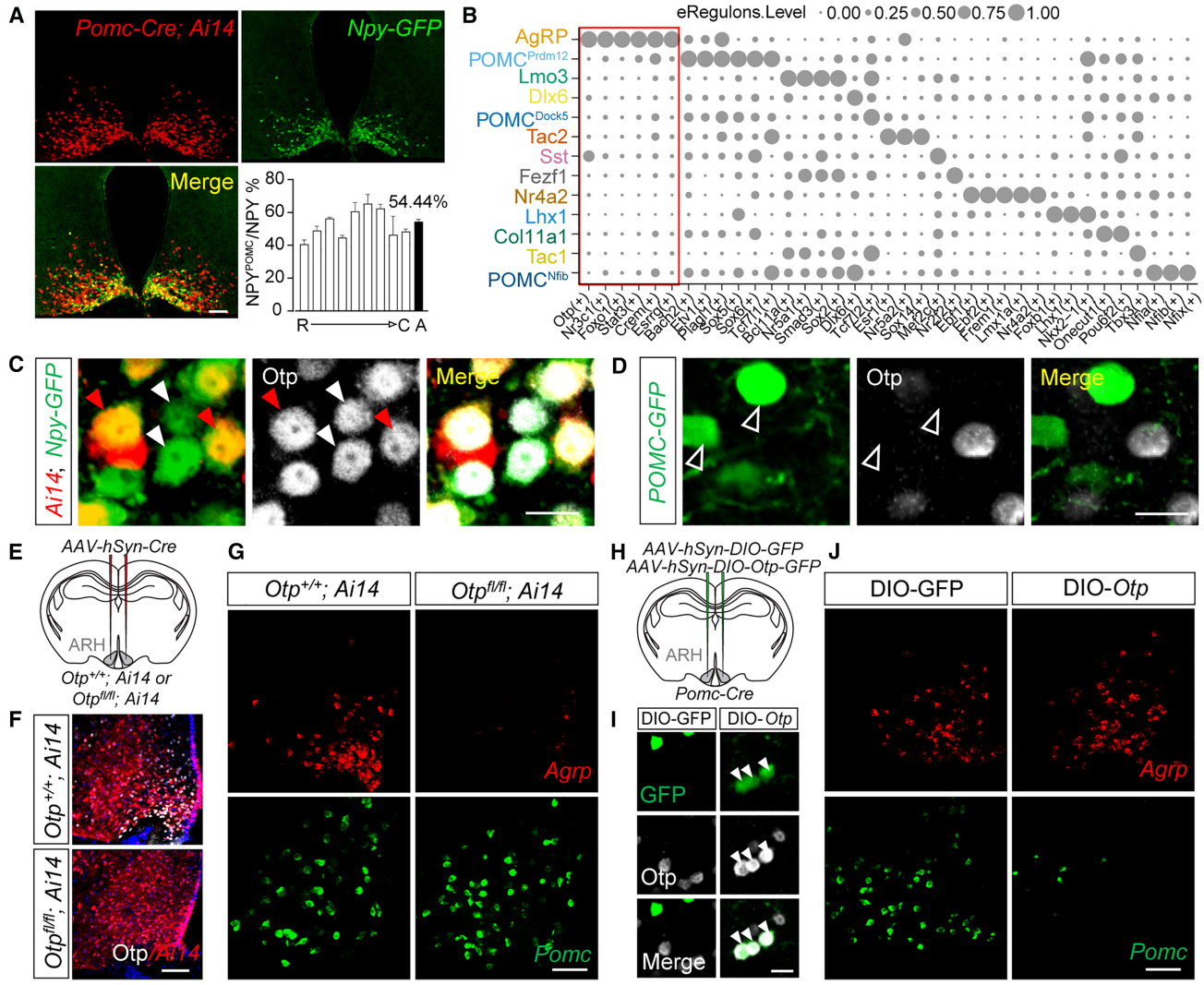

Figure 2. *Otp* is necessary for *Agrp* expression in the adult ARH

(A) Immunofluorescence of tdTomato (Ai14) and Npy-GFP in the ARH of adult *Pomc-Cre; Ai14; Npy-GFP* mice. PL neurons are labeled by *Pomc-Cre*-activated tdTomato (red), and Npy-GFP (green) marks adult AgRP neurons. POMC-derived AgRP neurons (yellow) co-express tdTomato and Npy-GFP. The bottom-right panel shows the percentage of POMC-derived AgRP neurons along the rostral-to-caudal axis (n = 3 mice). R, rostral; C, caudal; A, average. Scale bar: 100 μm.

(B) Single-Cell rEgulatory Network Inference and Clustering Plus (SCENIC$^+$) GRN enrichment dot plot. Circle size represents regulon activity per cell type. The red rectangle highlights six transcription factors enriched in POMC-derived AgRP neurons.

(C) Immunostaining showing Otp (white) in AgRP neurons in the adult ARH. POMC-derived AgRP neurons (yellow; red arrowheads) and non-POMC-derived AgRP neurons (green; white arrowheads) are labeled. Scale bar: 20 μm.

(D) Immunostaining showing that none of the POMC-GFP (green; hollow white arrowheads) neurons express Otp protein (white) in the adult ARH. Scale bar: 20 μm.

(E) Schematic of bilateral *AAV-Cre* virus injections into the ARH of *Otp$^{+/+}$; Ai14* or *Otp$^{fl/fl}$; Ai14* mice.

(F) Immunostaining of Otp (white) and tdTomato fluorescence (red) in the ARH. Scale bar: 50 μm.

(G) RNAscope analysis of *Agrp* (red) and *Pomc* (green) mRNAs in the ARH of *Otp$^{+/+}$* and *Otp$^{fl/fl}$* mice following *AAV-Cre* injection. Scale bar: 50 μm.

(H) Schematic of bilateral *AAV-d*ouble-floxed inverse orientation (*DIO*)*-GFP* or *AAV-DIO-Otp-GFP* virus injections into the ARH of *Pomc-Cre* mice.

(I) Immunostaining of Otp (white) and immunofluorescence of GFP in the ARH. White arrowheads indicate ectopic Otp expression in *Pomc-Cre* neurons. Scale bar: 20 μm.

(J) RNAscope analysis of *Agrp* (red) and *Pomc* (green) mRNAs in the ARH of *Pomc-Cre* mice following *AAV-DIO-GFP* or *AAV-DIO-Otp-GFP* injection. Scale bar: 50 μm.

See also Figures S6–S8.

Please cite this article in press as: Xu et al., Developmental reprogramming in melanocortin neurons modulates diet-induced obesity in mice, Neuron (2025), https://doi.org/10.1016/j.neuron.2025.12.022

CellPress
OPEN ACCESS

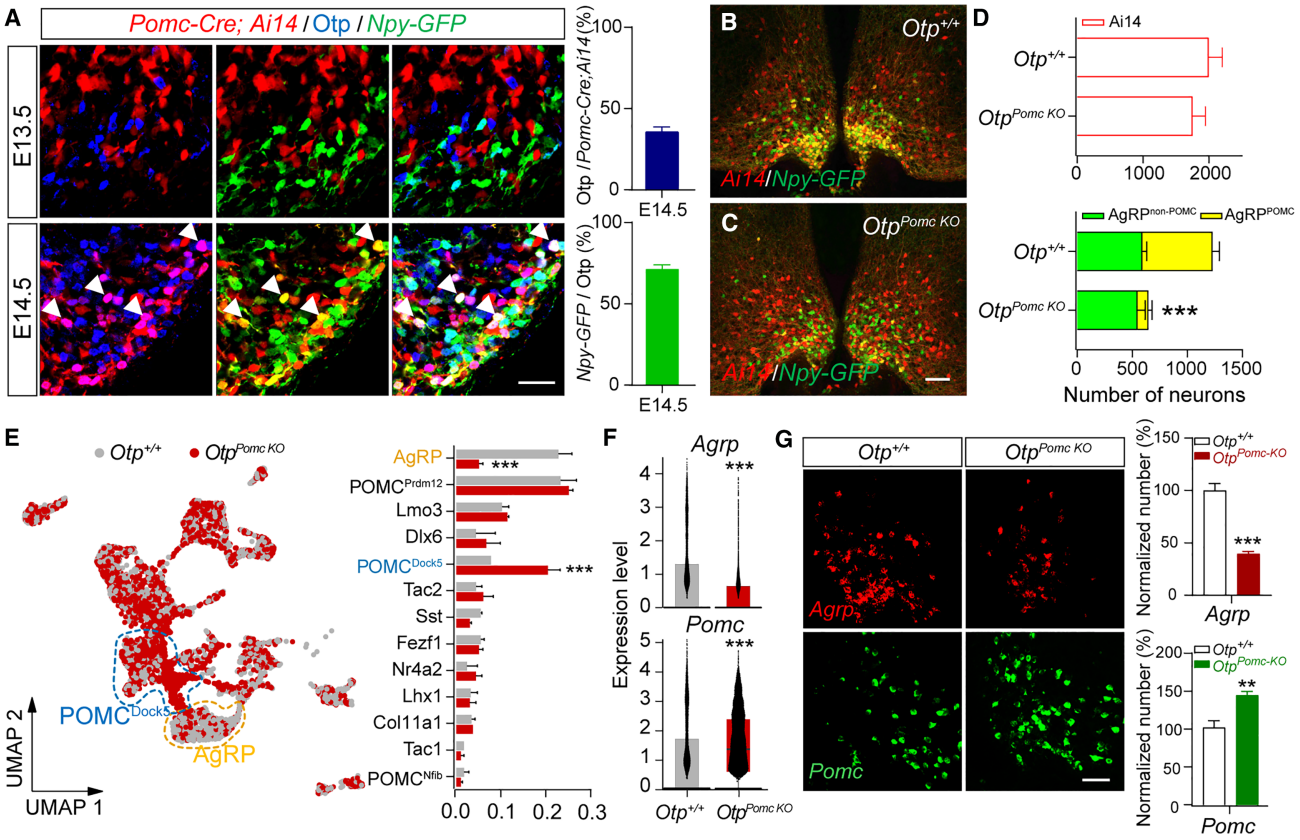

Figure 3. *Otp* is required for the POMC→AgRP fate switch

(A) Immunostaining of Otp (blue) in the ARH of E13.5 and E14.5 *Pomc-Cre*, *Ai14*, and *Npy-GFP* embryos. *Pomc* precursors are labeled by *Pomc-Cre* activated tdTomato (Ai14, red), and Npy-GFP (green) marks prospective AgRP neurons. White arrowheads indicate Otp expression in POMC-derived AgRP neurons at E14.5. Scale bar: 25 μm. Quantification of Otp$^+$ *Pomc* precursors and *Npy*-GFP$^+$ *Otp*-expressing neurons (71.3% ± 2.7%) is shown on the right (n = 6 mice).

(B and C) Immunofluorescence of tdTomato (Ai14, red) and GFP (green) in the ARH of adult *Otp*$^{+/+}$ (B) and *Otp*$^{Pomc\ KO}$ (C) mice. PL neurons are labeled by *Pomc-Cre* activated tdTomato (Ai14, red). POMC-derived AgRP neurons are shown in yellow, and non-POMC-derived AgRP neurons are shown in green. Scale bar: 100 μm.

(D) Quantification of the numbers of PL neurons (red; upper), non-POMC-derived AgRP neurons (green; lower), and POMC-derived AgRP neurons (yellow; lower) in the ARH of *Otp*$^{+/+}$ and *Otp*$^{Pomc\ KO}$ mice (n = 3 mice). Cell counts were performed on every fifth section collected along the rostral-to-caudal axis of the ARH. Two-way ANOVA with Sidak's post hoc test: F(1, 4) = 36, $p < 0.01$.

(E) Left: UMAP plot showing PL neuron distribution in *Otp*$^{+/+}$ and *Otp*$^{Pomc\ KO}$ mice. The POMC^{Dock5} cluster (blue dashed circle) expanded, while the AgRP cluster (yellow dashed circle) decreased in *Otp*$^{Pomc\ KO}$ mice. Right: quantification of the proportion of PL neuron clusters in *Otp*$^{+/+}$ and *Otp*$^{Pomc\ KO}$ mice. Two-way ANOVA with Sidak's post hoc test: F(1, 3) = 0.05, p = 0.83.

(F) Bar plots showing relative *Agrp* and *Pomc* expression levels in *Otp*$^{+/+}$ and *Otp*$^{Pomc\ KO}$ mice.

(G) RNAscope analysis of *Agrp* (red) and *Pomc* (green) in the ARH of *Otp*$^{+/+}$ and *Otp*$^{Pomc\ KO}$ mice. Scale bar: 50 μm. Quantification of normalized *Agrp*$^+$ and *Pomc*$^+$ neurons is shown on the right (n = 5 mice).

See also Figure S9.

populations, adult *Otp*$^{Pomc\ KO}$ mice exhibited increased *Pomc* expression and reduced *Agrp* expression in the ARH (Figures 3F and 3G), with similar effects observed in both male and female mice (Figure S9).

The developmental POMC-to-AgRP fate switch regulates obesity susceptibility in adulthood

Chow-fed *Otp*$^{Pomc\ KO}$ mice had comparable body weight to their littermate (*Otp*$^{fl/fl}$) controls (Figures S10A and S10B). However, when challenged with a high-fat diet (HFD), they gained less body weight and fat mass (Figures 4A and 4B). Metabolic cage analyses of 12-week-old females revealed that control mice developed hyperphagia upon transition from chow to HFD, whereas this response was blunted in *Otp*$^{Pomc\ KO}$ mice (Figure 4C). Energy expenditure or physical activity did not differ between the genotypes (Figures 4D and 4E). Notably, protection against HFD-induced weight gain was more pronounced in female *Otp*$^{Pomc\ KO}$ mice, whereas the effect was milder in males (Figure 4F). Consistently, metabolic cage analyses of age-matched male mice (12 weeks old) showed comparable food intake between *Otp*$^{Pomc\ KO}$ and control mice before the divergence in body weight (Figures S10C–S10E).

Given that both male and female *Otp*$^{Pomc\ KO}$ mice exhibited similar cellular and transcriptional changes, what mechanisms

Please cite this article in press as: Xu et al., Developmental reprogramming in melanocortin neurons modulates diet-induced obesity in mice, Neuron (2025), https://doi.org/10.1016/j.neuron.2025.12.022

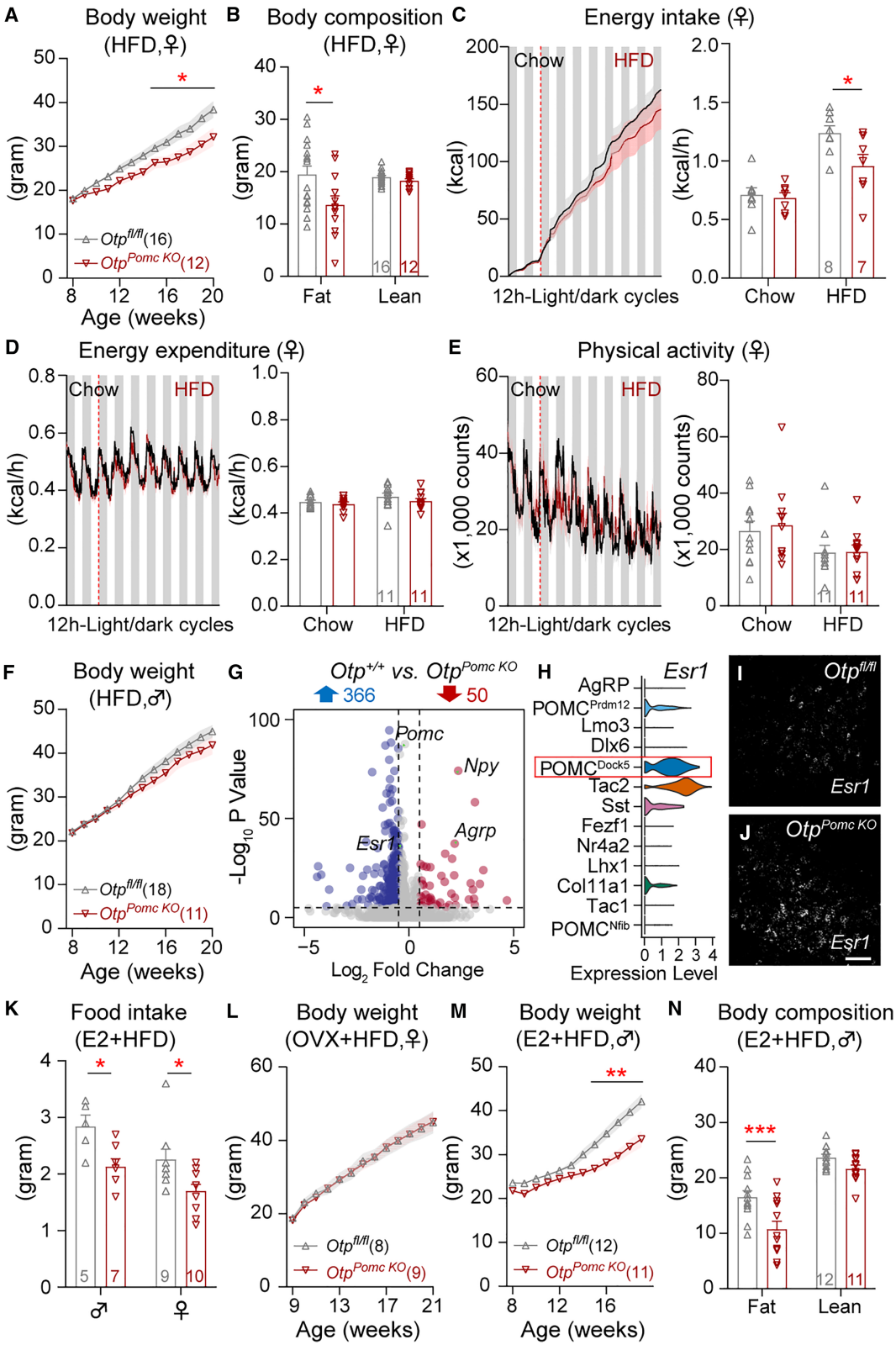

(legend on next page)

Please cite this article in press as: Xu et al., Developmental reprogramming in melanocortin neurons modulates diet-induced obesity in mice, Neuron (2025), https://doi.org/10.1016/j.neuron.2025.12.022

might underlie their sex-dimorphic differences in body weight regulation? Differential expression analyses between $Otp^{Pomc\ KO}$ and control mice identified estrogen receptor α (*Esr1*, encoding ERα), a receptor for the sex hormone estrogen, as one of the upregulated genes in both male and female $Otp^{Pomc\ KO}$ mice (Figures 4G, S10F, and S10G). The sexual dimorphic effect of estrogen on food intake is mediated, in part, by ERα in POMC neurons.[22,23] Notably, ERα is highly expressed in $POMC^{Dock5}$ neurons (Figure 4H). Consistent with the expansion of this cluster, we observed increased ERα expression in the ARH of $Otp^{Pomc\ KO}$ mice (Figures 4I and 4J). Moreover, an intraperitoneal dose of 17-β-estradiol produced a stronger anorexigenic effect in male and female $Otp^{Pomc\ KO}$ mice fed a HFD (Figure 4K), whereas this effect was absent under chow-fed conditions (Figure S10H).

Female $Otp^{Pomc\ KO}$ mice exhibited normal circulating estrogen levels, regular estrous cycles, and comparable luteinizing hormone (LH) expression in the anterior pituitary (Figure S11). Given the naturally higher estrogen levels in females, enhanced ERα signaling may contribute to the stronger protection against HFD-induced weight gain observed in female $Otp^{Pomc\ KO}$ mice. Supporting this interpretation, ovariectomy blunted the weight-loss phenotype in female $Otp^{Pomc\ KO}$ mice (Figure 4L), whereas chronic dietary supplementation with 17-β-estradiol amplified this effect in male $Otp^{Pomc\ KO}$ mice (Figures 4M and 4N).

DISCUSSION

Using single-nucleus multi-omics, we systematically characterized PL neurons in the adult hypothalamus and found that *Pomc* precursors give rise to multiple ARH and VMH neuronal subtypes with diverse physiological functions.

Yu et al. previously profiled *Pomc*-expressing neurons during embryonic and early postnatal stages using *Pomc-DsRed* mice.[5] Despite differences in developmental timing and genetic models, the neuronal clusters identified by Yu et al. align closely with corresponding POMC-derived subpopulations in our dataset. Remarkably, fewer than one-third of PL neurons retain *Pomc* expression into adulthood. The adult *Pomc*-expressing clusters differ in *Pomc* level—$POMC^{Prdm12}$ neurons show high *Pomc* expression, whereas $POMC^{Dock5}$ and $POMC^{Nfib}$ neurons exhibit lower levels—consistent with recent single-cell analyses of mature POMC neurons.[10] These cross-validations across independent datasets underscore the robustness of key neuronal populations and highlight the developmental and functional heterogeneity of PL neurons in the mediobasal hypothalamus.

Our findings have important implications for studies using *Pomc-Cre* mice. We show that *Pomc-Cre* targets a broader population of neurons, including three previously unrecognized VMH subtypes, than previously appreciated. Moreover, genes commonly assumed to function primarily in POMC neurons are also expressed in other PL-derived neurons. Therefore, our findings may necessitate a careful re-evaluation of prior studies using *Pomc*-Cre and underscore the importance of employing refined genetic tools to target specific neuronal subtypes with greater precision.

We further identify a developmental program that balances two functionally antagonistic feeding neurons. The onset of *Otp* expression in *Pomc* precursors is essential for the POMC-to-AgRP fate switch. In the absence of *Otp*, *Pomc* precursors fail to adopt AgRP/NPY identity, resulting in the loss of POMC-derived AgRP neurons and a concomitant expansion of $POMC^{Dock5}$ neurons. Thus, *Otp* acts as a critical molecular determinant orchestrating the POMC-to-AgRP transition.

Beyond its developmental role, *Otp* remains required to maintain *Agrp* expression in the adult hypothalamus. Ectopic *Otp* expression in mature POMC neurons suppresses *Pomc* but fails to induce *Agrp*, indicating that adult POMC neurons have lost developmental plasticity. Consistently, although both *Pomc-Cre* and $Pomc\text{-}CreER^{T2}$ transgenes are driven by the same bacterial artificial chromosome sequences,[24] fate mapping using the constitutively active *Pomc-Cre* labels multiple hypothalamic neuronal subtypes, whereas tamoxifen-induced *Cre* activity in adult $Pomc\text{-}CreER^{T2}$ mice selectively marks *Pomc*-expressing neurons.[25]

The developmental switch from POMC to AgRP identity has lasting metabolic consequences. $Otp^{Pomc\ KO}$ mice displayed reduced food intake and resistance to diet-induced obesity, revealing the functional importance of this fate switch in energy balance. While

Figure 4. The developmental POMC→AgRP fate switch regulates energy balance in adulthood

(A) Body weight curves in HFD-fed female mice. Two-way ANOVA with Sidak's post hoc test, $F(1, 26) = 5.36$, $p < 0.05$.
(B) Body composition. Two-way ANOVA with Sidak's post hoc test, $F(1, 26) = 5.27$, $p < 0.05$.
(C) Left: continuous traces of cumulative food intake in metabolic cages, binned into 12-h light and dark phases, before and after the dietary switch (red dashed line). Right: daily averages of food intake. Two-way ANOVA with Sidak's post hoc test, $F(1, 13) = 5.20$, $p < 0.05$.
(D) Left: continuous traces of energy expenditure in metabolic cages. Right: daily averages of energy expenditure. Two-way ANOVA with Sidak's post hoc test, $F(1, 20) = 0.93$, $p = 0.35$.
(E) Left: continuous traces of physical activity in metabolic cages. Right: daily averages of physical activity. Two-way ANOVA with Sidak's post hoc test, $F(1, 20) = 0.02$, $p = 0.90$.
(F) Body weight curves in HFD-fed male mice. Two-way ANOVA with Sidak's post hoc test, $F(1, 27) = 1.38$, $p = 0.25$.
(G) Volcano plot of differentially expressed genes ($\log_2$ fold change > 0.5; adjusted p value < 0.05) between $Otp^{+/+}$ and $Otp^{Pomc\ KO}$ mice. Downregulated genes are shown in red, and upregulated genes are shown in blue. Gene counts are indicated above.
(H) Violin plot showing *Esr1* expression across different PL neuron clusters.
(I and J) RNAscope analysis of *Esr1* mRNA in the ARH of $Otp^{fl/fl}$ (I) and $Otp^{Pomc\ KO}$ (J) mice. Scale bar: 50 μm.
(K) Average daily food intake in HFD-fed male and female mice after an intraperitoneal dose of 17-β-estradiol (0.5 μg). Two-way ANOVA with Sidak's post hoc test, $F(1, 27) = 14.68$, $p < 0.001$.
(L) Body weight curves of HFD-fed ovariectomized female mice. Two-way ANOVA with Sidak's post hoc test, $F(1, 15) = 0.01$, $p = 0.92$.
(M) Body weight curves of HFD-fed male mice with dietary 17-β-estradiol supplementation. Two-way ANOVA with Sidak's post hoc test, $F(1, 21) = 11.57$, $p < 0.01$.
(N) Body composition. Two-way ANOVA with Sidak's post hoc test, $F(1, 22) = 9.97$, $p < 0.01$.
See also Figures S10 and S11

excessive consumption of HFDs promotes obesity, diet-induced hyperphagia is a conserved adaptive behavior across species, enabling rapid energy storage when food availability fluctuates. Given the established role of melanocortin neurons in mediating hyperphagic responses,[26] the POMC-to-AgRP transition likely represents a fundamental component of this evolutionary adaptation. However, biological mechanisms optimized for ancestral survival can become maladaptive in modern environments characterized by chronic caloric abundance. Consistent with this view, disruption of this switch limits diet-induced hyperphagia and confers protection against obesity.

The blunted hyperphagic response in $Otp^{Pomc\ KO}$ mice is unlikely to result from reduced orexigenic peptides, as *Agrp* or *Npy* knockouts show minimal feeding phenotypes.[27] Instead, the expansion of $POMC^{Dock5}$ neurons and elevated *Pomc* expression likely increase anorexigenic tone. Notably, protection from diet-induced obesity was sexually dimorphic, with females showing a more pronounced effect. This difference correlates with increased *Esr1* expression—a key mediator of estrogen's anorexigenic actions—revealing a link between developmental plasticity, sex hormones, and long-term metabolic regulation. These findings align with previous studies demonstrating that *Esr1* acts in POMC neurons to suppress food intake.[22,23] Building on this, our data further pinpoint $POMC^{Dock5}$ neurons as a potential site mediating estrogen's effect on feeding and body weight. Although cell-type-specific manipulation of *Esr1* in $POMC^{Dock5}$ neurons is not yet feasible, pharmacological modulation of estrogen signaling altered the sex-dependent phenotype in $Otp^{Pomc\ KO}$ mice. These systemic interventions were designed to assess the overall contribution of estrogen signaling rather than to test whether *Esr1* alone is sufficient to restore the phenotype. Together, our results suggest that broad transcriptional and cellular remodeling—rather than a single effector gene—underlies the metabolic adaptations observed in $Otp^{Pomc\ KO}$ mice.

Our findings open several avenues for future investigation. It will be important to determine how environmental factors, such as maternal overnutrition or undernutrition, shape these developmental fate-switch programs. Further studies should test whether Otp directly binds regulatory elements controlling *Agrp* activation or *Pomc* repression. Moreover, because melanocortin neurons participate in both homeostatic and hedonic feeding,[28,29] it will be of interest to examine whether *Otp* deletion alters food preference or reward-driven feeding beyond satiety regulation.

RESOURCE AVAILABILITY

Lead contact

Requests for further information, resources, and reagents should be directed to and will be fulfilled by the lead contact, Chen Liu (chen.liu@utsouthwestern.edu).

Materials availability

All materials generated in this study are available upon request from the lead contact.

Data and code availability

- The raw and processed single-nucleus multiome data generated in this study are available at Gene Expression Omnibus (GEO): GSE287161.
- The code used for bioinformatic analyses in this study can be accessed at Zenodo (https://doi.org/10.5281/zenodo.17916507).
- Additional information required to reanalyze the data is available from the lead contact upon request.

ACKNOWLEDGMENTS

C.L. was supported by US NIH grants R01 DK114036, DK130892, and DK136592. L.L. was supported by a postdoctoral fellowship (23POST1019715) and a Career Development Award (24CDA1257999) from the American Heart Association. We thank members of the UTSW Metabolic Phenotyping Core, which was supported by the UTSW NORC grant under NIDDK/NIH award number P30DK127984.

AUTHOR CONTRIBUTIONS

B.X., L.L., and C.L. designed the experiments. B.X., L.L., X.C., R.W., A.G.A., S.C.W., and S. collected data. B.X., L.L., M.C., Z.W., and C.L. analyzed the data. B.X., L.L., and C.L. wrote the manuscript.

DECLARATION OF INTERESTS

The authors declare no competing interests.

STAR★METHODS

Detailed methods are provided in the online version of this paper and include the following:

- KEY RESOURCES TABLE
- EXPERIMENTAL MODEL AND STUDY PARTICIPANT DETAILS
  - Animals
- METHOD DETAILS
  - Immunostaining and RNAscope
  - Metabolic phenotype analysis
  - Assessment of estrous cycles
  - Estradiol feeding study
  - Ovariectomy
  - Body weight and composition measurements
  - Stereotaxic surgery
  - Single-nuclei multiome seq
  - Single-nuclei multiome seq analysis
- QUANTIFICATION AND STATISTICAL ANALYSIS

SUPPLEMENTAL INFORMATION

Supplemental information can be found online at https://doi.org/10.1016/j.neuron.2025.12.022.

Received: June 25, 2025
Revised: November 6, 2025
Accepted: December 16, 2025

REFERENCES

1. Sweeney, P., Gimenez, L.E., Hernandez, C.C., and Cone, R.D. (2023). Targeting the central melanocortin system for the treatment of metabolic disorders. Nat. Rev. Endocrinol. *19*, 507–519. https://doi.org/10.1038/s41574-023-00855-y.
2. Hahn, T.M., Breininger, J.F., Baskin, D.G., and Schwartz, M.W. (1998). Coexpression of Agrp and NPY in fasting-activated hypothalamic neurons. Nat. Neurosci. *1*, 271–272. https://doi.org/10.1038/1082.
3. Padilla, S.L., Carmody, J.S., and Zeltser, L.M. (2010). Pomc-expressing progenitors give rise to antagonistic neuronal populations in hypothalamic feeding circuits. Nat. Med. *16*, 403–405. https://doi.org/10.1038/nm.2126.

4. McNay, D.E.G., Pelling, M., Claxton, S., Guillemot, F., and Ang, S.L. (2006). Mash1 is required for generic and subtype differentiation of hypothalamic neuroendocrine cells. Mol. Endocrinol. *20*, 1623–1632. https://doi.org/10.1210/me.2005-0518.

5. Yu, H., Rubinstein, M., and Low, M.J. (2022). Developmental single-cell transcriptomics of hypothalamic POMC neurons reveal the genetic trajectories of multiple neuropeptidergic phenotypes. eLife *11*, e72883. https://doi.org/10.7554/eLife.72883.

6. Padilla, S.L., Reef, D., and Zeltser, L.M. (2012). Defining POMC neurons using transgenic reagents: impact of transient Pomc expression in diverse immature neuronal populations. Endocrinology *153*, 1219–1231. https://doi.org/10.1210/en.2011-1665.

7. McHugh, T.J., Jones, M.W., Quinn, J.J., Balthasar, N., Coppari, R., Elmquist, J.K., Lowell, B.B., Fanselow, M.S., Wilson, M.A., and Tonegawa, S. (2007). Dentate gyrus NMDA receptors mediate rapid pattern separation in the hippocampal network. Science *317*, 94–99. https://doi.org/10.1126/science.1140263.

8. Mo, A., Mukamel, E.A., Davis, F.P., Luo, C., Henry, G.L., Picard, S., Urich, M.A., Nery, J.R., Sejnowski, T.J., Lister, R., et al. (2015). Epigenomic Signatures of Neuronal Diversity in the Mammalian Brain. Neuron *86*, 1369–1384. https://doi.org/10.1016/j.neuron.2015.05.018.

9. Li, L., Xu, B., and Liu, C. (2023). Sample enrichment for single-nucleus sequencing using concanavalin A-conjugated magnetic beads. Star Protoc. *4*, 102595. https://doi.org/10.1016/j.xpro.2023.102595.

10. Leon, S., Simon, V., Lee, T.H., Steuernagel, L., Clark, S., Biglari, N., Lesté-Lasserre, T., Dupuy, N., Cannich, A., Bellocchio, L., et al. (2024). Single cell tracing of Pomc neurons reveals recruitment of 'Ghost' subtypes with atypical identity in a mouse model of obesity. Nat. Commun. *15*, 3443. https://doi.org/10.1038/s41467-024-47877-2.

11. Lam, B.Y.H., Cimino, I., Polex-Wolf, J., Nicole Kohnke, S., Rimmington, D., Iyemere, V., Heeley, N., Cossetti, C., Schulte, R., Saraiva, L.R., et al. (2017). Heterogeneity of hypothalamic pro-opiomelanocortin-expressing neurons revealed by single-cell RNA sequencing. Mol. Metab. *6*, 383–392. https://doi.org/10.1016/j.molmet.2017.02.007.

12. Campbell, J.N., Macosko, E.Z., Fenselau, H., Pers, T.H., Lyubetskaya, A., Tenen, D., Goldman, M., Verstegen, A.M.J., Resch, J.M., McCarroll, S.A., et al. (2017). A molecular census of arcuate hypothalamus and median eminence cell types. Nat. Neurosci. *20*, 484–496. https://doi.org/10.1038/nn.4495.

13. Kong, D., Tong, Q., Ye, C., Koda, S., Fuller, P.M., Krashes, M.J., Vong, L., Ray, R.S., Olson, D.P., and Lowell, B.B. (2012). GABAergic RIP-Cre neurons in the arcuate nucleus selectively regulate energy expenditure. Cell *151*, 645–657. https://doi.org/10.1016/j.cell.2012.09.020.

14. Martinez de Morentin, P.B., Gonzalez, J.A., Dowsett, G.K.C., Martynova, Y., Yeo, G.S.H., Sylantyev, S., and Heisler, L.K. (2024). A brainstem to hypothalamic arcuate nucleus GABAergic circuit drives feeding. Curr. Biol. *34*, 1646–1656.e4. https://doi.org/10.1016/j.cub.2024.02.074.

15. Qi, Y., Lee, N.J., Ip, C.K., Enriquez, R., Tasan, R., Zhang, L., and Herzog, H. (2023). Agrp-negative arcuate NPY neurons drive feeding under positive energy balance via altering leptin responsiveness in POMC neurons. Cell Metab. *35*, 979–995.e7. https://doi.org/10.1016/j.cmet.2023.04.020.

16. Solheim, M.H., Stroganov, S., Chen, W., Subagia, P.S., Bauder, C.A., Wnuk-Lipinski, D., Del Río-Martín, A., Sotelo-Hitschfeld, T., Beddows, C.A., Klemm, P., et al. (2025). Hypothalamic PNOC/NPY neurons constitute mediators of leptin-controlled energy homeostasis. Cell *188*, 3550–3566.e22. https://doi.org/10.1016/j.cell.2025.04.001.

17. Mittelman-Smith, M.A., Williams, H., Krajewski-Hall, S.J., Lai, J., Ciofi, P., McMullen, N.T., and Rance, N.E. (2012). Arcuate kisspeptin/neurokinin B/dynorphin (KNDy) neurons mediate the estrogen suppression of gonadotropin secretion and body weight. Endocrinology *153*, 2800–2812. https://doi.org/10.1210/en.2012-1045.

18. Zhang, X., and van den Pol, A.N. (2016). Hypothalamic arcuate nucleus tyrosine hydroxylase neurons play orexigenic role in energy homeostasis. Nat. Neurosci. *19*, 1341–1347. https://doi.org/10.1038/nn.4372.

19. Long, H.K., Prescott, S.L., and Wysocka, J. (2016). Ever-Changing Landscapes: Transcriptional Enhancers in Development and Evolution. Cell *167*, 1170–1187. https://doi.org/10.1016/j.cell.2016.09.018.

20. Bravo González-Blas, C., De Winter, S., Hulselmans, G., Hecker, N., Matetovici, I., Christiaens, V., Poovathingal, S., Wouters, J., Aibar, S., and Aerts, S. (2023). SCENIC+: single-cell multiomic inference of enhancers and gene regulatory networks. Nat. Methods *20*, 1355–1367. https://doi.org/10.1038/s41592-023-01938-4.

21. Chen, X., Wyler, S.C., Li, L., Arnold, A.G., Wan, R., Jia, L., Landy, M.A., Lai, H.C., Xu, P., and Liu, C. (2020). Comparative Transcriptomic Analyses of Developing Melanocortin Neurons Reveal New Regulators for the Anorexigenic Neuron Identity. J. Neurosci. *40*, 3165–3177. https://doi.org/10.1523/JNEUROSCI.0155-20.2020.

22. Xu, Y., Nedungadi, T.P., Zhu, L., Sobhani, N., Irani, B.G., Davis, K.E., Zhang, X., Zou, F., Gent, L.M., Hahner, L.D., et al. (2011). Distinct hypothalamic neurons mediate estrogenic effects on energy homeostasis and reproduction. Cell Metab. *14*, 453–465. https://doi.org/10.1016/j.cmet.2011.08.009.

23. Ye, H., Yang, X., Feng, B., Luo, P., Torres Irizarry, V.C., Carrillo-Sáenz, L., Yu, M., Yang, Y., Eappen, B.P., Munoz, M.D., et al. (2024). 27-Hydroxycholesterol acts on estrogen receptor alpha expressed by POMC neurons in the arcuate nucleus to modulate feeding behavior. Sci. Adv. *10*, eadi4746. https://doi.org/10.1126/sciadv.adi4746.

24. Berglund, E.D., Liu, C., Sohn, J.W., Liu, T., Kim, M.H., Lee, C.E., Vianna, C.R., Williams, K.W., Xu, Y., and Elmquist, J.K. (2013). Serotonin 2C receptors in pro-opiomelanocortin neurons regulate energy and glucose homeostasis. J. Clin. Investig. *123*, 5061–5070. https://doi.org/10.1172/JCI70338.

25. Caron, A., Dungan Lemko, H.M., Castorena, C.M., Fujikawa, T., Lee, S., Lord, C.C., Ahmed, N., Lee, C.E., Holland, W.L., Liu, C., and Elmquist, J.K. (2018). POMC neurons expressing leptin receptors coordinate metabolic responses to fasting via suppression of leptin levels. eLife *7*, e33710. https://doi.org/10.7554/eLife.33710.

26. Yeo, G.S.H., Chao, D.H.M., Siegert, A.M., Koerperich, Z.M., Ericson, M.D., Simonds, S.E., Larson, C.M., Luquet, S., Clarke, I., Sharma, S., et al. (2021). The melanocortin pathway and energy homeostasis: From discovery to obesity therapy. Mol. Metab. *48*, 101206. https://doi.org/10.1016/j.molmet.2021.101206.

27. Qian, S., Chen, H., Weingarth, D., Trumbauer, M.E., Novi, D.E., Guan, X., Yu, H., Shen, Z., Feng, Y., Frazier, E., et al. (2002). Neither agouti-related protein nor neuropeptide Y is critically required for the regulation of energy homeostasis in mice. Mol. Cell. Biol. *22*, 5027–5035. https://doi.org/10.1128/MCB.22.14.5027-5035.2002.

28. Cassano, D.A., Barrile, F., Reynaldo, M., Fernandez, G., Cornejo, M.P., Tolosa, M.J., Heredia, M.F., Ferreira, N., Fideles, H.J., De Francesco, P.N., et al. (2025). AgRP neuron activity enhances reward-related consummatory behaviors during energy deficit in mice. Commun. Biol. *8*, 1152. https://doi.org/10.1038/s42003-025-08620-9.

29. Alhadeff, A.L., Goldstein, N., Park, O., Klima, M.L., Vargas, A., and Betley, J.N. (2019). Natural and Drug Rewards Engage Distinct Pathways that Converge on Coordinated Hypothalamic and Reward Circuits. Neuron *103*, 891–908.e6. https://doi.org/10.1016/j.neuron.2019.05.050.

30. Xu, B., Lawler, K., Wyler, S.C., Li, L., Swati, Keogh, J.M., Chen, X., Wan, R., Almeida, A.G., Kirsch, S., et al. (2025). Orthopedia regulates melanocortin 4 receptor transcription and energy homeostasis. Sci. Transl. Med. *17*, eadr6459. https://doi.org/10.1126/scitranslmed.adr6459.

31. Schindelin, J., Arganda-Carreras, I., Frise, E., Kaynig, V., Longair, M., Pietzsch, T., Preibisch, S., Rueden, C., Saalfeld, S., Schmid, B., et al. (2012). Fiji: an open-source platform for biological-image analysis. Nat Methods *9*, 676–682. https://doi.org/10.1038/nmeth.2019.

32. Li, L., Wyler, S.C., León-Mercado, L.A., Xu, B., Oh, Y., Swati, Chen, X., Wan, R., Arnold, A.G., Jia, L., et al. (2022). Delineating a serotonin 1B receptor circuit for appetite suppression in mice. J. Exp. Med. *219*, e20212307. https://doi.org/10.1084/jem.20212307.

Please cite this article in press as: Xu et al., Developmental reprogramming in melanocortin neurons modulates diet-induced obesity in mice, Neuron (2025), https://doi.org/10.1016/j.neuron.2025.12.022

STAR★METHODS

KEY RESOURCES TABLE

REAGENT or RESOURCE	SOURCE	IDENTIFIER
Antibodies		
Rabbit polyclonal anti-OTP	Sigma	Cat# HPA039365; RRID: AB_10674423
Rabbit polyclonal anti-RFP	Rockland	Cat# 600-401-379; RRID: AB_2209751
Rabbit polyclonal anti-Caspase3	Cell Signaling Technology	Cat# 9661; RRID: AB_2341188
TotalSeq™-A0451 anti-NPC Hashtag 1 Antibody	BioLegend	Cat# 682205; RRID: AB_2861054
TotalSeq™-A0452 anti-NPC Hashtag 2 Antibody	BioLegend	Cat# 682207; RRID: AB_2861055
TotalSeq™-A0453 anti-NPC Hashtag 3 Antibody	BioLegend	Cat# 682209; RRID: AB_2861056
Bacterial and virus strains		
AAV8-hSyn-GFP	UNC Vector Core	N/A
AAV8-hSyn-Cre-GFP	UNC Vector Core	N/A
AAV9-hSyn-DIO-GFP	BrainVTA	Cat# PT-1103
AAV9-hSyn-DIO-Otp-GFP	BrainVTA	Cat# PT-11892
Chemicals, peptides, and recombinant proteins		
fetal bovine serum	Invitrogen	Cat# 10270106
DPBS	Invitrogen	Cat# 14190-144
Sucrose	Fisher Chemical	Cat# S5-500
Tris-HCl, 1 M	Sigma-Aldrich	Cat# T2194
NaCl Solution, 5 M	Sigma-Aldrich	Cat# 59222C
DTT solution	Sigma-Aldrich	Cat# 646563
BSA	Sigma-Aldrich	Cat# A7979
Tween-20	Sigma-Aldrich	Cat# P9416
cOmplete™, EDTA-free Protease Inhibitor Cocktail Tablet	Sigma-Aldrich	Cat# 11873580001
1 M HEPES solution	Sigma-Aldrich	Cat# H0887
1 M KCl solution	Sigma-Aldrich	Cat# 60142
Triton X-100	Sigma-Aldrich	Cat# T8787
Glycerol	Sigma-Aldrich	Cat# G5516
1 M $MnCl_2$ solution	Sigma-Aldrich	Cat# M1787
16% paraformaldehyde	Electron Microscopy Sciences	Cat# 15710S
Isoflurane 99.9%	Covetrus	Cat# 11695-6777-1
17-ß-estradiol-3-benzoate	Sigma	Cat# E8515
17-ß-estradiol pellets	Innovative Research of America	Cat# NE-121
Critical commercial assays		
RNAscope™ Multiplex Fluorescent V2 Assay	ACD	Cat# 323270
Single Cell Multiome ATAC + Gene Expression	10X Genomics	Cat# 1000285
Chromium Next GEM Chip J Single Cell	10X Genomics	Cat# 1000230
Mouse Estradiol Rapid ELISA Kit	Invitrogen	Cat# EELR013
Deposited data		
Raw and analyzed data	This paper	GEO: GSE287161
Experimental models: Organisms/strains		
Mouse: C57BL/6J wild type	JAX	Cat# 000664; RRID: IMSR_JAX:000664
Mouse: Pomc-Cre	JAX	Cat# 005965; RRID: IMSR_JAX:005965
Mouse: Npy-GFP	JAX	Cat# 006417; RRID: IMSR_JAX:006417
Mouse: POMC-GFP	JAX	Cat# 009593; RRID: IMSR_JAX:009593

(*Continued on next page*)

Continued

REAGENT or RESOURCE	SOURCE	IDENTIFIER
Mouse: Rosa26-Ai14-CAG-LSL-TdTom	JAX	Cat# 007914; RRID: IMSR_JAX:007914
Mouse: Rosa26- CAG-Sun1/sfGFP	JAX	Cat# 021039; RRID: IMSR_JAX:021039
Mouse: Otp$^{fl/fl}$	Xu et al.[30]	N/A
Software and algorithms		
Cellranger-arc	10X Genomics	https://www.10xgenomics.com
Seurat - R	Rahul Satija	https://github.com/satijalab/seurat
Prism	GraphPad	https://www.graphpad.com
ImageJ	Schindelin et al.[31]	https://imagej.nih.gov/ij/
Custom code in this study	This paper	https://doi.org/10.5281/zenodo.17916507
Other		
regular chow	Harlan-Teklad	Cat# 2916
high-fat diet (HFD)	Research Diets Inc.	Cat# D12492i

EXPERIMENTAL MODEL AND STUDY PARTICIPANT DETAILS

Animals

All mice were housed in a temperature and humidity-controlled room with a 12-h light/12-h dark cycle (lights on at 6:00 a.m., lights off at 6:00 p.m.) in the animal facility of the University of Texas Southwestern Medical Center. Food and water were supplied *ad libitum*. Mice were fed with either regular chow (Harlan-Teklad, 2916, 4.25% kcal from fat) or a high-fat diet (Research Diets Inc., D12492i, 60% kcal from fat). All experimental procedures were approved by the Institutional Animal Care and Use Committee (IACUC) at the University of Texas Southwestern Medical Center. All mice used were maintained on a C57BL/6 background. Experimental animals ranged in age from embryonic day 13 to 12 months, and both sexes were used. Commercial mouse lines were: *Pomc-Cre* (JAX, #005965); *Npy-GFP* (JAX, #006417); *POMC-GFP* (JAX, #009593); *Rosa26-Ai14-CAG-LSL-TdTom* (JAX, # 007914); and *Rosa26-CAG-Sun1/sfGFP* (JAX, # 021039) mice were purchased from The Jackson Laboratory. *Otp$^{fl/fl}$* mice were generated by CRISPR-Cas9-mediated gene editing at the fertilized one-cell stage and more details were described previously.[30]

METHOD DETAILS

Immunostaining and RNAscope

Details for performing these experiments were described previously.[21,32] Briefly, mouse brains were fixed in 4% paraformaldehyde overnight and then were sectioned by a vibratome (Leica VT1000S). The primary antibodies used include anti-OTP (Sigma, rabbit, #HPA039365); anti-Caspase3 (Cell Signaling Technology, rabbit, #9661) and anti-RFP (Rockland, rabbit, #600-401-379). Secondary antibodies (AlexaFluor-488, -594, or -647) were from Thermo Fisher Scientific. RNAscope was performed using ACD RNAscope Multiplex Fluorescent Detection Kit version 2 following the manufacturer's (Advanced Cell Diagnostics) protocol with the following probes *Mm-Pomc (ACD #314081; ACD # 314081-C2), Mm-Prdm12 (ACD # 524371-C2), Mm-Dock5 (ACD # 872971-C3), Mm-Nfib (ACD # 586511-C3), Mm-Agrp (ACD # 400711-C2), Mm-Sst (ACD # 404631-C2), Mm-Dlx6 (ACD # 475021), Mm-Tac2 (ACD # 446391-C3), Mm-Nr4a2 (ACD # 423351-C3), Mm-Nr5a1 (ACD # 445731-C2), Mm-Lmo3 (ACD # 497631-C3), Mm-Fezf1 (ACD # 812321-C3), Mm-Tac1 (ACD # 410351-C3), Mm-Lepr (ACD # 552841-C2), Mm-Cnr1 (ACD # 420721-C3), Mm-Insr (ACD # 401011-C4), Mm-Htr2c (ACD # 401001-C2), Mm-Esr1 (ACD # 478201-C3), and Mm-Lhb (ACD # 478401-C3)*.

Metabolic phenotype analysis

To measure the energy intake and expenditure, 12-week-old, weight-matched mice were placed into an indirect calorimetric system (PhenoMaster; TSE Systems) in the Metabolic Phenotyping Core of UT Southwestern Medical Center. To measure the mouse estradiol, trunk blood was collected from anesthetized mice and processed to obtain plasma by centrifugation and assayed using a Mouse Estradiol (E2) ELISA kit (Invitrogen, EELR013) by the Metabolic Phenotyping Core of UT Southwestern Medical Center.

Assessment of estrous cycles

Eight-week-old chow-fed female mice were first confirmed to have undergone vaginal opening. Vaginal smears were collected daily at 3 p.m. using gentle lavage. Smear cytology was examined under a light microscope to identify the stage of the estrous cycle.

Estradiol feeding study

Estradiol benzoate (Sigma, E8515) was dissolved in corn oil. Male and female mice were fed with HFD or chow-diet and single-housed for 3 days for habituation and to obtain baseline measurements for body weight and food intake. After habituation, animals

Please cite this article in press as: Xu et al., Developmental reprogramming in melanocortin neurons modulates diet-induced obesity in mice, Neuron (2025), https://doi.org/10.1016/j.neuron.2025.12.022

were weighed and treated daily with 150 μL corn oil for 3 days and then with 0.5 μg estradiol (17-β-estradiol-3-benzoate) in 150 μL corn oil for 4 days via IP injections. Animals were monitored for food intake daily during the treatment.

The estradiol pellet (Innovative Research of America, 17-β-estradiol pellets, 0.25 mg, 90 Days, Catalog #: NE-121) was implanted subcutaneously in male mice at 8 weeks of age. The pellet implantation study was conducted under isoflurane anesthesia followed by carprofen analgesia. Male mice were fed with HFD after the procedure.

Ovariectomy

Adult female mice were bilaterally ovariectomized at 8 weeks of age. The procedure was applied under isoflurane anesthesia followed by carprofen analgesia. OVX female mice were fed with HFD after 1 week of recovery.

Body weight and composition measurements

Body weight was monitored weekly. In the HFD studies, mice were maintained on regular chow until at least 8 weeks old before being fed with HFD. Body composition was assessed using the magnetic-resonance whole-body composition analyzer (EchoMRI) at the end of the body weight monitoring.

Stereotaxic surgery

Male mice (at least 8 weeks old) were anesthetized with 1.5% isoflurane and placed on a stereotaxic frame (David Kopf Instruments). After the skull was exposed and leveled in the horizontal plane, small holes were drilled into the skull. AAV was bilaterally injected into the ARH (anteroposterior [AP], –1.55 mm; mediolateral [ML], ±0.25 mm; dorsoventral [DV], –5.85 mm). A total of 200 nL of the virus was injected at a rate of 20 nL/min and was allowed 8–10 min to diffuse before the injection needle was removed. AAV vectors used AAV8-hSyn-Cre-GFP (UNC Vector Core), AAV9-hSyn-DIO-GFP (BrainVTA, PT-1103) and AAV9-hSyn-DIO Otp-GFP (Brainvta, PT-11892).

Single-nuclei multiome seq

Tissue preparation, dissociation, and nuclei extraction were described in a STAR Protocol.[9] In this study, the ARH regions were dissected from adult *Pomc-Cre; Sun1/sfGFP* and *Pomc-Cre; Otp$^{fl/fl}$; Sun1/sfGFP* mice under a fluorescent dissecting microscope and immediately stored at -80°C. For each genotype, approximately 20 ARH samples, including both male and female mice, were pooled. Each pooled sample was homogenized in 1 mL of homogenization buffer using a Dounce grinder pestle. The homogenate solutions were centrifuged at 500 g for 5 min in a swing bucket rotor, and the supernatants were discarded. The nuclei were resuspended with 100 μl of wash buffer and incubated with different TotalSeq Hashtag antibodies against the nuclear pore complex (0.5 μl, BioLegend) for 10 min. Following incubation, the nuclei suspensions were washed three times with 1 mL of wash buffer and spun down at 500 g for 5 min. After hashtagging each sample with the antibody, samples were pooled together, and GFP-positive nuclei were sorted during FANS at the Flow Cytometry Core of UTSW Medical Center. After sorting, the nuclei solution was adjusted to the desired concentration at 500–2,000 nuclei/μl, then proceeded with the 10× Multiome kit at the UTSW Next Generation Sequencing Core. Libraries were sequenced on a NextSeq 2000 mid-throughput sequencing platform or BGI T7 sequencing platform.

Single-nuclei multiome seq analysis

Hashtag-count matrix was generated and demultiplexed from sequenced hashtag FASTQ reads using Cellranger-7.0.0. RNA UMI counts and ATAC peaks were obtained by aligning FASTQ files to the mouse reference genome (mm10) using CellrangerARC-2.0.2 from 10× Genomics.

The raw RNA count matrix and ATAC fragment data were further processed using R packages Seurat 5.0 and Signac 1.14, respectively. Peaks that overlapped with genomic blacklist regions for the mm10 genome were removed. Filtering based on RNA-assay metrics (300 < nFeature_RNA < 10,000, percent.mt <3) and ATAC-assay metrics (2,000 <nCount_ATAC < 100,000, nucleosome_signal <2, TSS.enrichment > 2, blacklist_fraction < 0.025 and pct_reads_in_peaks > 25). The filtered data were log normalized with a default size factor of 10,000. The expression of all the genes was scaled before the dimensional reduction.

For ATAC data integration, the fragments of 4 ATAC libraries were first combined and then re-analyzed using the CallPeaks function (MACS3). The ATAC layers were integrated using the FindIntegrationAnchors function.

For RNA data integration, mitochondrial genes (*mt-Nd1*, *mt-Nd2*, *mt-Co1*, *mt-Co2*, *mt-Atp8*, *mt-Atp6*, *mt-Co3*, *mt-Nd3*, *mt-Nd4l*, *mt-Nd4*, *mt-Nd5*, *mt-Nd6*, *mt-Cytb*) and sex-linked gene *Xist* were removed, then RNA layers were integrated using FindIntegrationAnchors function.

RNA and ATAC modalities were integrated using FindMultiModalNeighbors at parameters of 50 principal component (PC) dimensions. Clusters were annotated with a shared nearest-neighbor modularity optimization-based clustering algorithm with a resolution of 0.15. Non-linear dimensionality reduction was visualized with Uniform Manifold Approximation and Projection (UMAP). ''FindAllMarkers'' was used to find genes with significant differential expression of each cluster with default parameters.

SCENIC+ was used to analyze transcription factor regulatory programs. Raw counts were imported along with cluster annotations. RNA counts were log-normalized, scaled, and filtered to highly variable genes. Raw ATAC reads were imported and peaks were called normalized to the size of each chromosome using MACS2 before being filtered using the mm10 blacklist. Consensus peaks were

Please cite this article in press as: Xu et al., Developmental reprogramming in melanocortin neurons modulates diet-induced obesity in mice, Neuron (2025), https://doi.org/10.1016/j.neuron.2025.12.022

converted to a bed file for downstream analysis. Processed RNA and ATAC data were subjected to QC controlling for fragment count, FRIP, TSS enrichment, and duplication rate to filter to high-quality cells. CisTopic was used to perform latent Dirichlet allocation topic modeling before PyCisTarget was used to identify enriched motifs and differentially accessible regions. These results were used as inputs to the SCENIC+ algorithm against a list of all known mouse transcription factors from the HUST database. Estimated gene regulatory networks were used for downstream analysis.

QUANTIFICATION AND STATISTICAL ANALYSIS

Sample sizes were chosen to reliably measure experimental parameters while remaining in compliance with ethical guidelines for minimizing animal use, and they were similar to those reported in previous publications. Replicate information is indicated in the figure legends. All results are presented as mean ± SEM and analyzed using statistical tools implemented in Prism (GraphPad, version 10). Statistical analyses were performed using the Student's *t* test and two-way analysis of variance (ANOVA). Differences with $p < 0.05$ were considered to be significant. $p < 0.05$ (*), $p < 0.01$ (**), and $p < 0.001$ (***).

Neuron, Volume *114*

Supplemental information

Developmental reprogramming in melanocortin neurons modulates diet-induced obesity in mice

Baijie Xu, Li Li, Meilin Chen, Zan Wu, Xiameng Chen, Swati, Rong Wan, Amanda G. Almeida, Steven C. Wyler, and Chen Liu

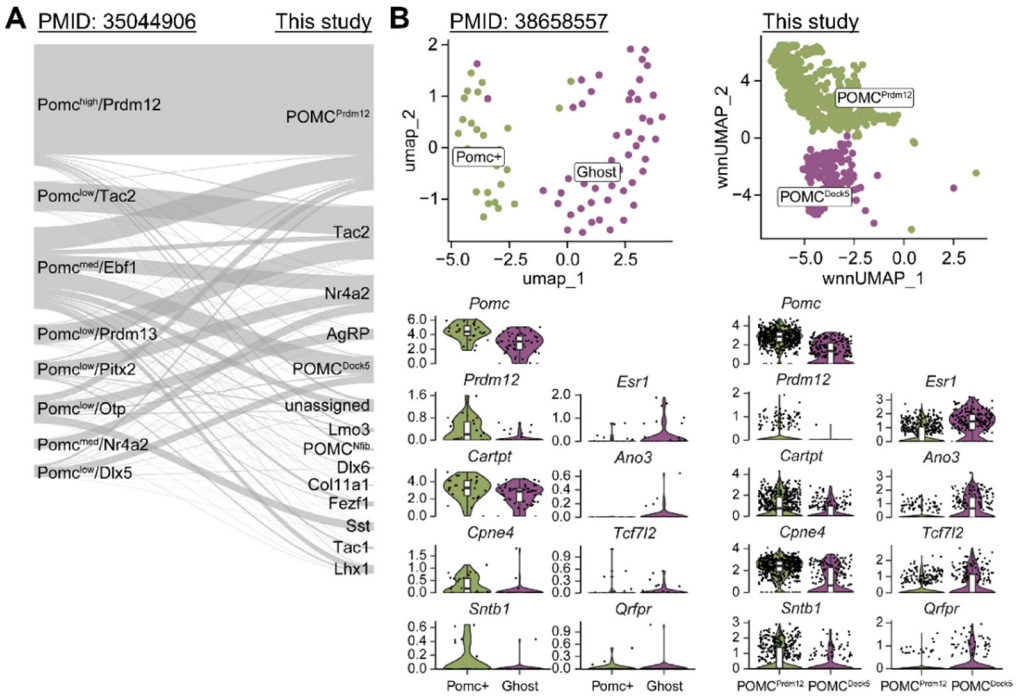

Figure S1. Cross-validation of published single-cell transcriptome datasets of developing and mature *Pomc*-expressing neurons, related to Figure 1

(A) Comparison of *Pomc*-expressing neuron clusters during embryonic and early postnatal stages in *Pomc-DsRed* mice (PMID: 35044906) and PL neuron clusters in this study using *Pomc-Cre; Sun1-sfGFP* mice.

(B) Dimensional reduction plots showing mature POMC neuron clusters identified in adult *Pomc*-CreER^{T2} mice (left, PMID: 38658557) and in *Pomc*-Cre mice (right, this study). Similar gene expression patterns are observed between the Pomc^{+} and POMC^{Prdm12} clusters, as well as between the Ghost and POMC^{Dock5} clusters.

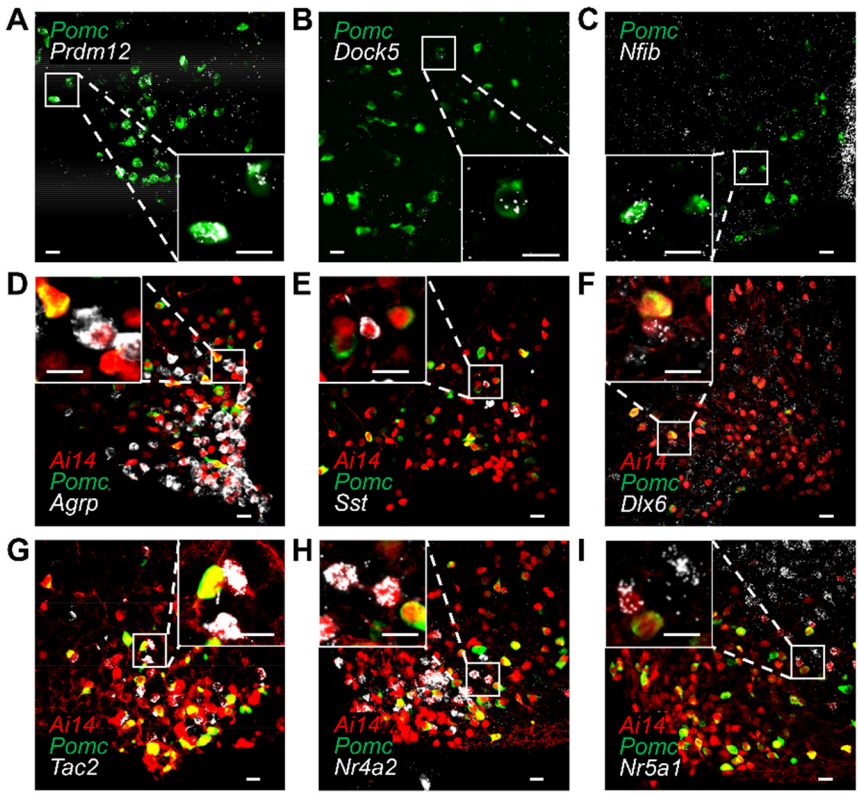

Figure S2. Validation of gene expression in POMC-derived neurons in the adult mouse mediobasal hypothalamus, related to Figure 1

(A-C) RNAscope analysis showing co-expression of *Pomc* with *Prdm12* (A), *Dock5* (B), and *Nfib* (C) mRNAs in individual neurons. Squares indicate regions enlarged in **Figure 1D**. Scale bar: 20 μm.

(D-F) RNAscope analysis showing *Pomc* mRNA (green), *Pomc-Cre* activated tdTomato (Ai14) fluorescence (red), and mRNAs (white) for *Agrp* (D), *Sst* (E), and *Dlx6* (F). Squares indicate regions enlarged in **Figure 1E**. Scale bar: 20 μm.

(G-I) RNAscope analysis showing *Pomc* mRNA (green), *Pomc-Cre* activated tdTomato (Ai14) fluorescence (red), and mRNAs (white) for *Tac2* (G), *Nr4a2* (H), and *Nr5a1* (I). Squares indicate regions enlarged in **Figures 1F-1H**. Scale bar: 20 μm.

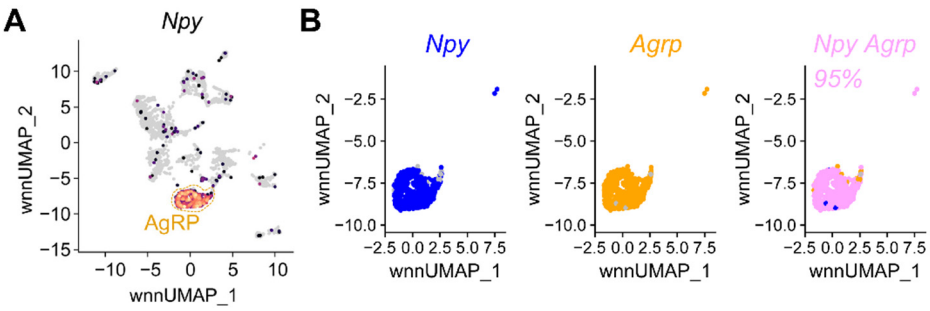

Figure S3. Expression analysis of *Npy* and *Agrp* in POMC-derived neurons, related to Figure 1

(A) Expression of *Npy* across PL neuron clusters. The AgRP cluster is outlined by a yellow dashed line.

(B) Co-expression patterns of *Npy* and *Agrp* within POMC-derived AgRP neurons. Pink indicates double-positive neurons, which constitute 95% of the population.

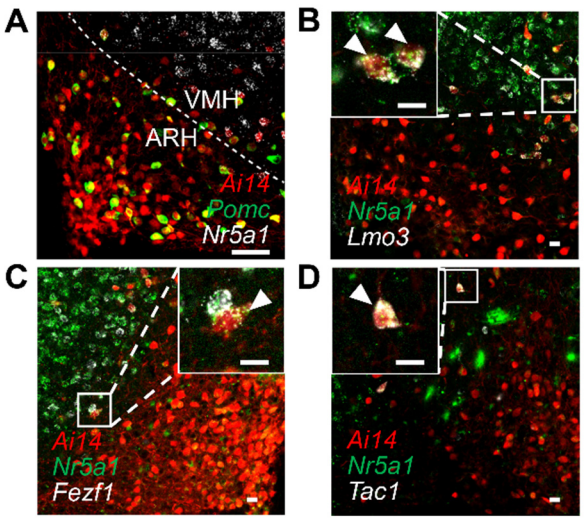

Figure S4. Expression of VMH neuron marker *Nr5a1* in a subset of PL neurons, related to Figure 1

(A) RNAscope analysis showing *Pomc* and *Nr5a1* mRNAs in PL neurons in the adult mediobasal hypothalamus. PL neurons are labeled by *Pomc-Cre*-activated tdTomato (Ai14) fluorescence. The dashed line indicates the boundary between the ARH and VMH. Scale bar: 50 μm.

(B-D) RNAscope analysis showing co-expression of *Nr5a1* with *Lmo3* (B), *Fezf1* (C), and *Tac1* (D) in adult mediobasal hypothalamic neurons. Squares indicate enlarged regions, and arrowheads mark individual double-positive PL neurons. Scale bars: 20 μm.

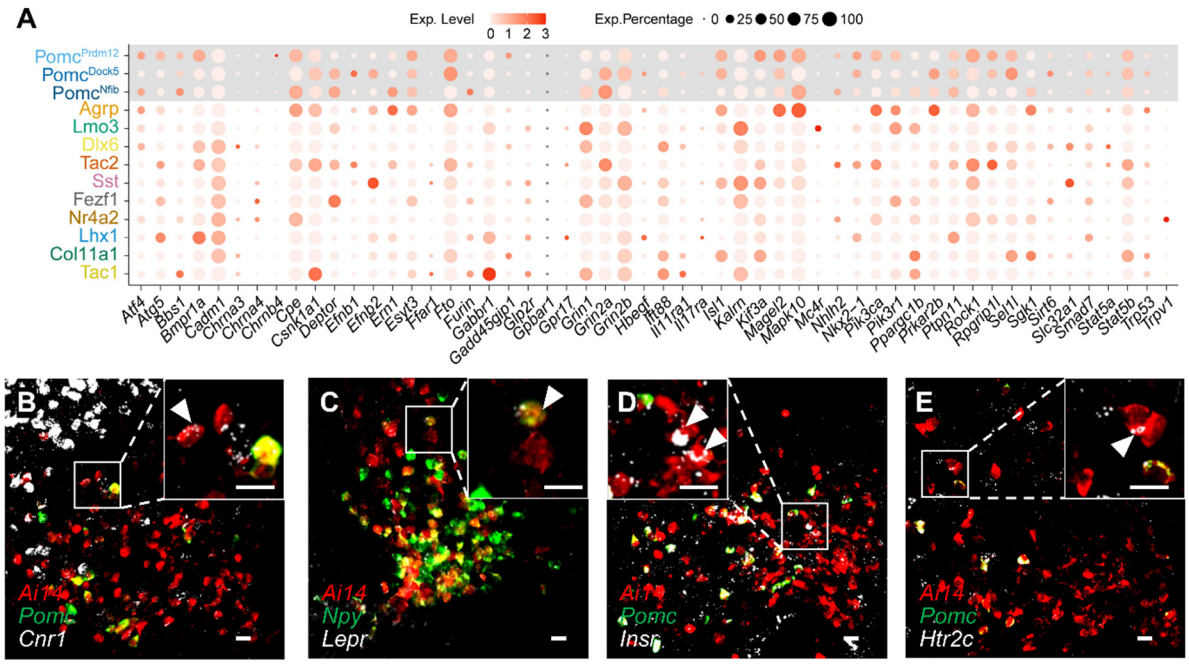

Figure S5. Expression patterns of *Pomc-Cre*-targeted genes in PL neurons, related to Figure 1

(A) Dot plot illustrating the relative expression of genes targeted by *Pomc-Cre* across PL neuron clusters, continuing from **Figure 1I**. Dot size represents the percentage of expressing cells, and color intensity indicates expression level (light: low; dark: high).

(B-E) RNAscope analyses showing expression of *Cnr1* (B), *Lepr* (C), *Insr* (D), and *Htr2c* (E) in adult mediobasal hypothalamic neurons. Squares indicate enlarged regions, and arrowheads mark the individual non-POMC PL neurons. Scale bars: 20 μm.

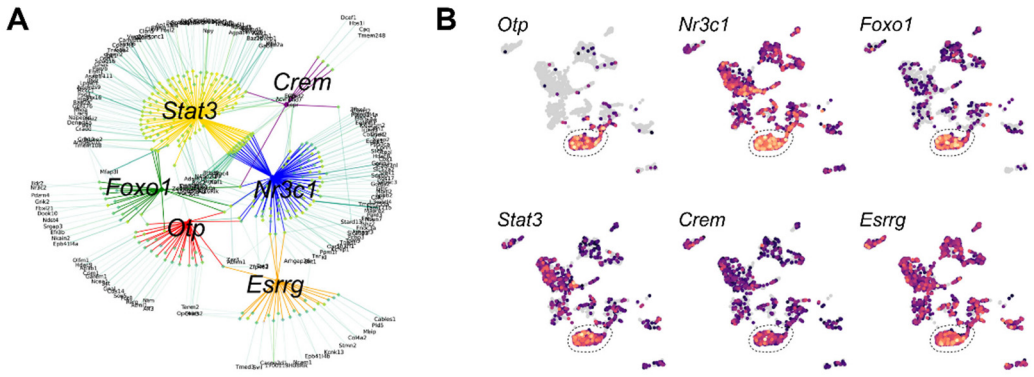

Figure S6. GRNs regulated by six transcription factors in POMC-derived AgRP neurons, related to Figure 2

(A) Visualization of GRNs regulated by *Otp*, *Nr3c1*, *Foxo1*, *Stat3*, *Crem*, and *Esrrg* using SCENIC+ analysis.

(B) Feature plots showing the expression of each transcription factors across PL neuron clusters. The dashed line outlines the AgRP cluster.

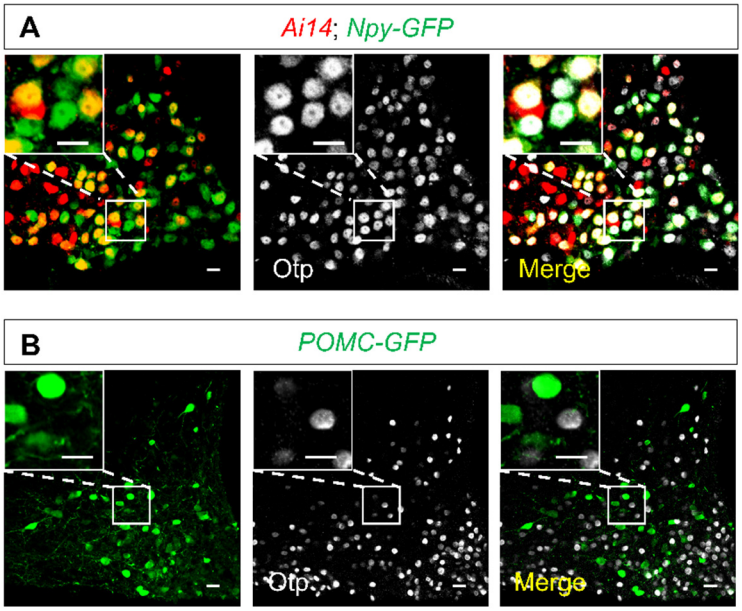

Figure S7. Otp expression in adult ARH neurons, related to Figure 2

(A) Immunostaining showing Otp (white) in AgRP neurons in the adult ARH. Squares indicate regions enlarged in **Figure 2C**. Scale bar: 20 μm.

(B) Immunostaining showing Otp (white) in POMC neurons in the adult ARH. Squares indicate regions enlarged in **Figure 2D**. Scale bar: 20 μm.

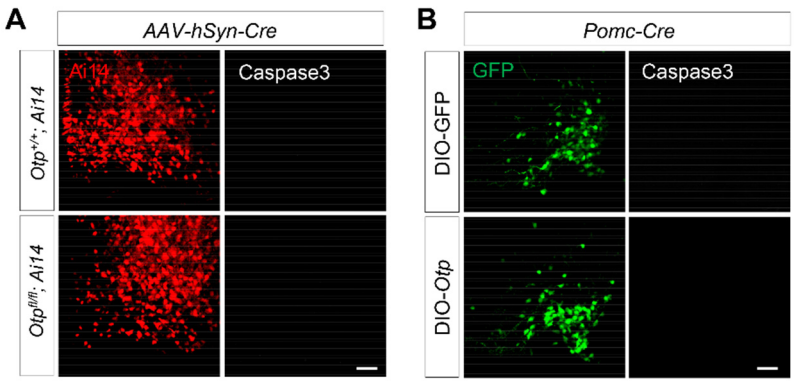

Figure S8. Assessment of cell death after *Otp* deletion or overexpression in the ARH, related to Figure 2

(A) Immunostaining of Caspase3 (white) and tdTomato fluorescence (red; indicates the *AAV-hSyn-Cre*-infected neurons) in the ARH of $Otp^{+/+}$*; Ai14* and $Otp^{fl/fl}$*; Ai14* mice. Scale bar: 50 μm.

(B) Immunostaining of Caspase3 (white) and immunofluorescence of GFP (green; indicates the POMC neurons after *Otp* overexpression) in the ARH of *Pomc-Cre* mice. Scale bar: 50 μm.

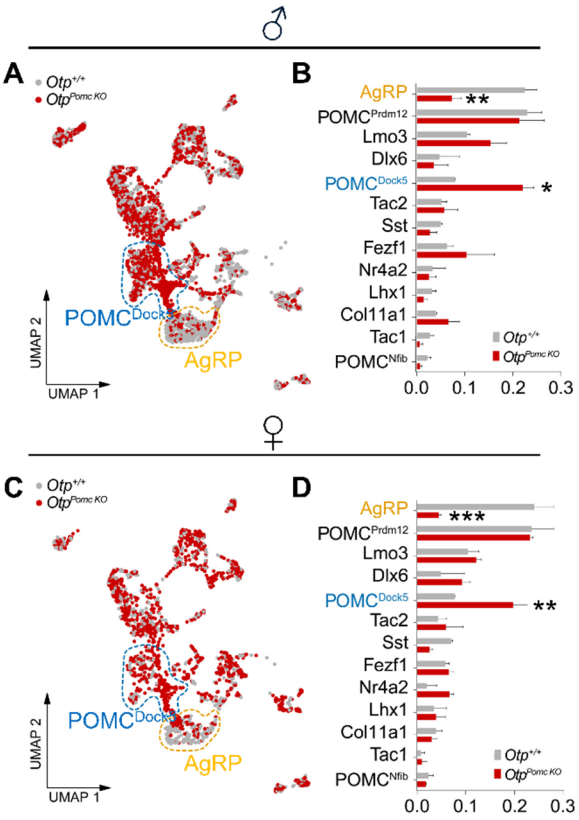

Figure S9. Cellular and molecular changes in male and female *Otp*$^{Pomc\ KO}$ mice, related to Figure 3

(A and C) UMAP plots showing PL neuron distributions in *Otp*$^{+/+}$ and *Otp*$^{Pomc\ KO}$ male (A) and female (C) mice. The POMC^{Dock5} cluster (blue dashed circle) expanded, while the AgRP cluster (yellow dashed circle) decreased in *Otp*$^{Pomc\ KO}$ mice.

(B and D) Quantification of the proportion of PL neuron clusters in *Otp*$^{+/+}$ and *Otp*$^{Pomc\ KO}$ male (B) and female (D) mice.

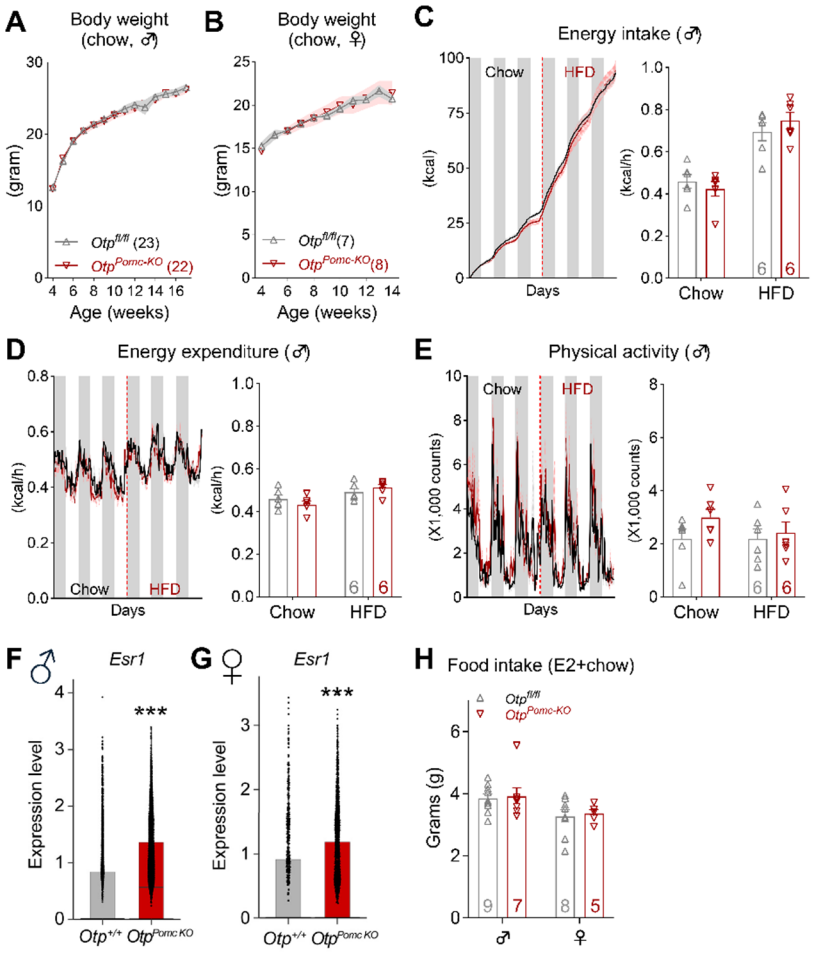

Figure S10. Body weight, energy balance, *Esr1* expression, and response to 17-β-estradiol in chow-fed *Otp*$^{+/+}$ and *Otp*$^{Pomc\ KO}$ mice of both sexes, related to Figure 4

(A and B) Body weight curves in chow-fed male (A) and female (B) mice.

(C) Left: Continuous traces of cumulative food intake in metabolic cages, binned into 12-hour light and dark phases, before and after the dietary switch (red dashed line). Right: Daily averages of food intake.

(D) Left: Continuous traces of energy expenditure in metabolic cages. Right: Daily averages of energy expenditure.

(E) Left: Continuous traces of physical activity in metabolic cages. Right: Daily averages of physical activity.

(F and G) Bar plots showing relative *Esr1* expression in *Otp*$^{+/+}$ and *Otp*$^{Pomc\ KO}$ male (F) and female (G) mice.

(H) Average daily food intake in chow-fed male and female mice after an intraperitoneal dose of 17-β-estradiol (0.5 µg).

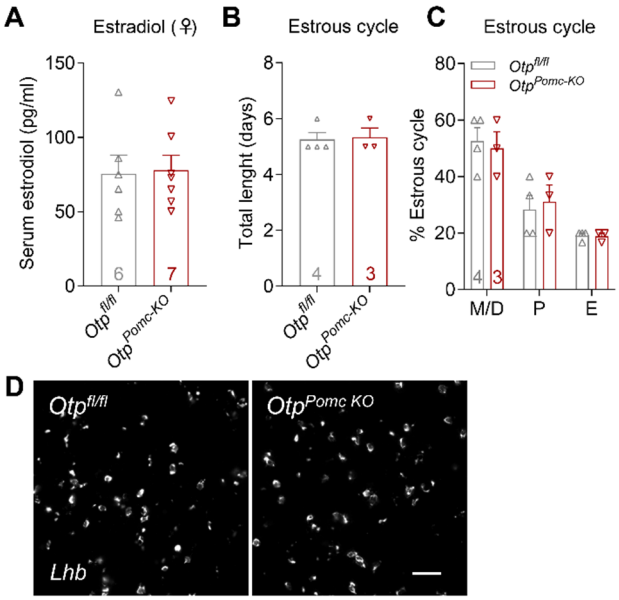

Figure S11. Evaluations of circulating estrogen levels, estrous cycles, and luteinizing hormone expression, related to Figure 4

(A) Baseline plasma estradiol levels in female *Otp*$^{fl/fl}$ and *Otp*$^{Pomc\ KO}$ mice.

(B) Total duration of estrous cycles in female *Otp*$^{fl/fl}$ and *Otp*$^{Pomc\ KO}$ mice.

(C) Relative length of metestrus/diestrus (M/D), proestrus (P), and estrus (E) phases within the entire estrous cycle.

(D) RNAscope analysis of *Lhb* mRNA in the anterior pituitary of *Otp*$^{fl/fl}$ and *Otp*$^{Pomc\ KO}$ mice. Scale bar: 50 μm.